

Chemical Vapor Deposition Synthesis and Optical Properties of Nb₂O₅ thin films with Hybrid Functional Theoretical Insight into Band Structure and Band Gaps

Sanjayan Sathasivam^{a,b}, Benjamin A. D. Williamson^c, Shaeel A. Althabaiti^{d,e}, Abdullah Y. Obaid^{d,e}, Sulaiman N. Basahel^{d,e}, Mohamed Mokhtar^{d,e}, David O. Scanlon^{c,f}, Claire J. Carmalt^a and Ivan P. Parkin^{a*}

*Corresponding author

^aMaterials Chemistry Centre, Department of Chemistry, University College London, 20 Gordon Street, London WC1H 0AJ, UK

Fax: (+44) 20-7679-7463

E-mail: i.p.parkin@ucl.ac.uk

^bBio Nano Consulting Ltd, The Gridiron Building, One Pancras Square, London N1C 4AG, UK

Fax: (+44) 20-7396-1056

^cKathleen Lonsdale Materials Chemistry, Department of Chemistry, University College London, 20 Gordon Street, London WC1H 0AJ, UK

^dChemistry Department, King Abdulaziz University, Saudi Arabia

^eSurface Chemistry and Catalytic Studies Group, King Abdulaziz University, Saudi Arabia

^fDiamond Light Source Ltd., Diamond House, Harwell Science and Innovation Campus, Didcot, Oxfordshire OX11 0DE, United Kingdom.

Abstract

Nb₂O₅ is an important material able to exist in many polymorphs with unique optical properties and morphologies that are dependent on the synthetic route. Here we report a novel ambient pressure chemical vapour deposition route to Nb₂O₅ *via* aerosol assisted chemical vapour deposition. The amorphous as deposited films were annealed in air to obtain the three most stable crystal structures - orthorhombic, tetragonal and monoclinic. The films were thoroughly characterized for their material

properties and an in depth study into the optical properties was carried out using state of the art hybrid functional theory that allowed more insight into the optical properties of the materials.

Keywords: Niobium oxide, CVD, polymorphs, density functional theory, band gap

Introduction

Niobium pentoxide (Nb_2O_5) is a wide band gap material that has attracted much interest of late due to its ability to exhibit various crystal phases that allow it to display many functional properties.¹ The band gap of Nb_2O_5 has been reported to vary from semiconducting (3.1 eV) to insulating (5.3 eV) range and can be adjusted through doping, changes in crystallinity and stoichiometry and heat treatment to obtain different phases.¹ The most stable phases of Nb_2O_5 are the orthorhombic (*o*), tetragonal (*t*) and monoclinic (*m*), usually activated *via* thermal treatment at 800, 1000 and 1100 °C respectively with typically an amorphous polymorph present below 500 °C.

Nb_2O_5 has been prepared in the thin film form by a range of techniques including reactive sputtering², pulsed laser deposition^{3,4}, atomic layer deposition⁵ and atmospheric pressure (AP) techniques such as AP-chemical vapour deposition⁶ and sol-gel dip coating⁷. The method of fabrication plays an important role in the morphological properties of the thin films and their application. Applications for Nb_2O_5 are wide ranging, for example nanostructured Nb_2O_5 has been used as a photoanode in dye sensitized solar cells due to its wide band gap, excellent electron injection efficiency and chemical stability.⁸⁻¹¹ Furthermore nanostructured high surface area layers are advantageous for sensing¹²⁻¹⁴, catalytic¹⁵ and battery^{16,17} devices. For optical coatings however smooth and featureless Nb_2O_5 films are required to minimize light scattering.¹⁸ It has been noted that the preparatory methods to Nb_2O_5 are highly influential on the morphology and hence on the functional properties.¹

Here we report a novel route to Nb_2O_5 using a specialized form of chemical vapour deposition called aerosol assisted CVD.¹⁹ This simple ambient pressure and easily scalable CVD technique delivers the necessary precursors that are dissolved in a suitable solvent to the heated substrate in the form of aerosol droplets.²⁰⁻²² This

precursor delivery method is key in that it enables the use of non-volatile precursors that are typically incompatible with traditional forms of CVD.²³

Utilizing AACVD and when necessary a post deposition annealing step, we set out to fabricate amorphous, orthorhombic (*o*), tetragonal (*t*) and monoclinic (*m*) forms of Nb₂O₅ determine the optical properties and compare to new hybrid density functional theory calculations. The results show the calculated band gaps match closely with the experimental results. The calculations also show density of states and band structures for all three of the crystalline phases. Furthermore, simulated valence band structures of the films have been presented and compared to experimental results.

Results and Discussion

AACVD was employed to prepare amorphous (*a*) Nb₂O₅ thin films on quartz substrates from a one pot solution of [Nb(OEt)₅] and methanol at 450 °C. The films were subsequently annealed at 800, 1000 and 1200 °C for 12 hours to obtain the orthorhombic (*o*), tetragonal (*t*) and monoclinic (*m*) crystal phases respectively. Visually, the films were generally transparent but with increasing annealing temperature they became hazier. All films were well adhered to the substrate and passed the ScotchTM test.²⁴

The X-ray diffraction (XRD) patterns and scanning electron microscopy (SEM) images, shown in Figure 1, reveal the impact of post deposition annealing temperature on the crystallinity and morphology of the Nb₂O₅ films. The as-deposited film was X-ray amorphous as evident from the lack of Bragg reflections in the XRD pattern (Figure 1a). Upon annealing under air at 800 °C peaks corresponding to the orthorhombic phase were seen. Similarly, *t*- and *m*- Nb₂O₅ films were obtained by annealing at 1000 °C and 1200 °C respectively. The XRD patterns also show all films to be phase pure with no evidence of mixed phase Nb₂O₅ composites formed. It can also be observed from the XRD patterns that there are some degrees of preferred orientation compared to the simulated patterns, this is most likely due strain caused by quartz substrate on the film during growth and annealing steps.

The differing morphology observed *via* SEM of the *a*-, *o*-, *t*-, *m*- Nb₂O₅ is shown in Figure 1b. The *a*-Nb₂O₅ film has a relatively flat morphology composed of densely packed spheres ~30 nm in diameter. In the *o*-Nb₂O₅ these spheres appear to have

coalesced together to form more structured features protruding from the substrate that range in size from 250 nm to 1000 nm. Parkin *et. al.* observed a similar morphology for *o*-Ta₂O₅ grown by AACVD and annealed at 800 °C. With further heat treatment, the morphology of the *t*-Nb₂O₅ shows similar morphology to *o*-Nb₂O₅ however with features between 1000 and 1200 nm in size. The *m*-Nb₂O₅ film shows a markedly different surface structure consisting of large rod like entities with some over 10 μm in length. The change in morphology to larger structural features with increasing annealing temperature as observed here is due to the increase in surface mobility during phase transformations that allows surfaces to reduce their total energy by reducing grain boundary area.

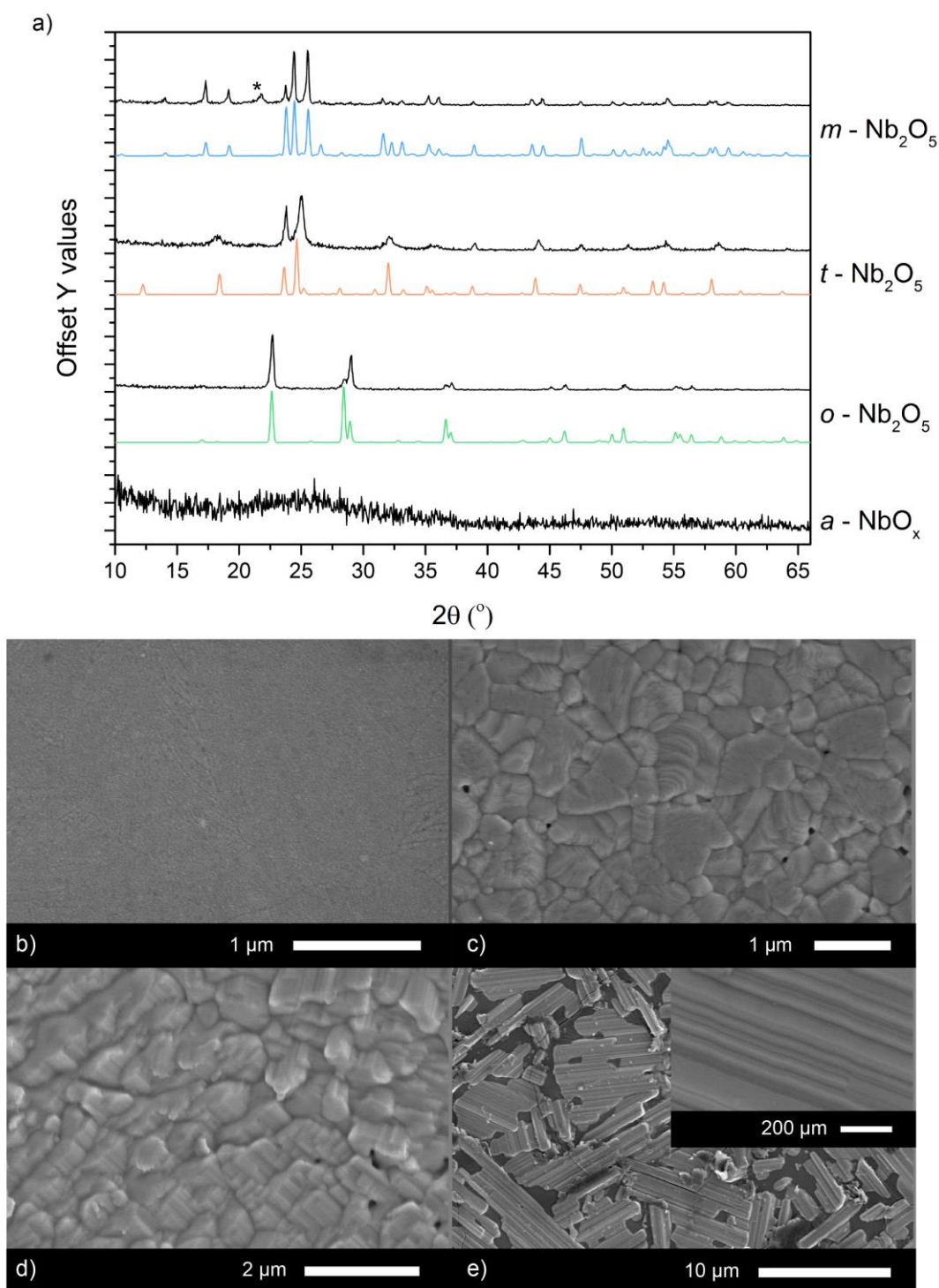


Figure 1: a) The XRD patterns of the as deposited and annealed films with the three crystal phases – orthorhombic (o), tetragonal (t) and monoclinic (m). The simulated patterns are in colour and the experimental in black. * Indicates peak due to the quartz substrate. The SEM micrographs of these films b) amorphous c) orthorhombic d) tetragonal and e) monoclinic are also shown.

Figure 2a-d shows the core level X-ray photoelectron spectroscopy (XPS) results for the four different Nb₂O₅ films. For the *a*-Nb₂O₅ (Figure 2a) the Nb 3d spectrum is

dominated by a simple spin orbit doublet separated by 2.8 eV with the $3d_{5/2}$ peak centered at 206.2 eV corresponding to literature reports for Nb(V). A weak low binding energy shoulder is also present which can be modelled to Nb(IV) (Nb $3d_{5/2}$ 204.7 eV) that arises from surface oxygen vacancies and has been seen previously for Nb₂O₅ samples.² This shoulder feature is not present in the annealed samples due to the oxidizing nature of the heat treatment. The annealed samples (Figure 2b-d) show only peaks corresponding to Nb(V) with Nb_{5/2} peak positions consistently at 206.6 eV, shifted to slightly higher binding energies relative to *a*-Nb₂O₅.

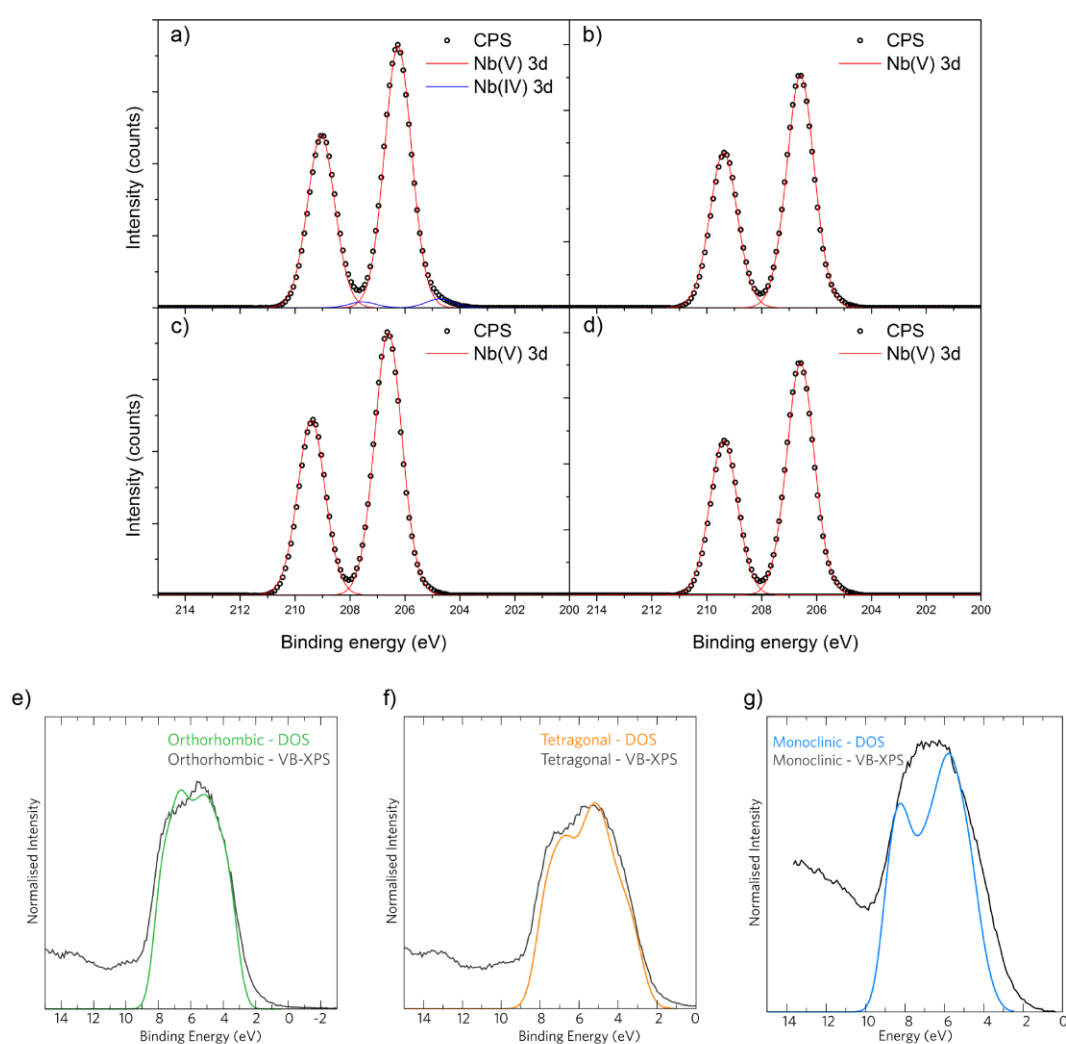


Figure 2: a) XPS spectra showing the Nb 3d transitions for the a) *a*-NbO_x b) *o*-Nb₂O₅ c) *t*-Nb₂O₅ d) *m*-Nb₂O₅ films on quartz. Two sets of doublets are observed in the Nb 3d spectrum for *a*-NbO_x suggests the presence of Nb⁵⁺ (95% abundance) and Nb⁴⁺ (5% abundance) oxidation state on the surface. The VB-XPS and simulated VB-XPS (colour) for e) *o*-Nb₂O₅, f) *t*-Nb₂O₅ and g) *m*-Nb₂O₅.

The experimental and simulated valence band (VB) XPS for the crystalline Nb₂O₅ films weighted using the atomic photoionisation cross-sections by Yeh and Lindau are shown in Figure 2e-g.²⁵ The experimental VB structure is composed of a broad feature made up of O 2*p* states that is centred at ~6 eV for the *o*- and *t*- Nb₂O₅ films but at ~9 eV for the high temperature monoclinic phase.² The calculated data is in good agreement with the experimental findings, in particular, there is an excellent correlation between the data sets for the orthorhombic and tetragonal structures. The peak widths for the orthorhombic, monoclinic and tetragonal VB-XPS in Figure 2 are ~8 eV, ~7 eV and 7 eV respectively. The simulated spectra for the monoclinic polymorph has a pronounced trough at a binding energy of ~9 eV arising from a lack of density of states that was not observed in the experimental data, however the slight troughs for the orthorhombic and tetragonal structures at ~6 eV were present in the experimental data as shoulders in the main peak. The slight discrepancies observed between the simulated and experimental VB XPS data (for example between 10-14 eV) mainly arise due to the measured XPS being of the surface while the calculated spectra are based on bulk Nb₂O₅.

The theoretical calculations for the three crystalline phases of Nb₂O₅ synthesised in this study were carried out using the HSE06 hybrid DFT functional using *ab-initio* methods. The calculated density of states (DOS) for each polymorph is provided in Figure 3, where, in each case the valence band maximum (VBM) is dominated by O 2*p* states. This behaviour is typical of most wide band gap oxides such as TiO₂ and In₂O₃. From ~ -6 eV to -4 eV in all three polymorphs, there is significant mixing between the Nb *d* states and the O 2*p* states with some minimal Nb *p* and *s* states. Between the energy ranges of -4eV to just below the VBM (0 eV) the amount of Nb *d* states begins to tail off with an increase in Nb *p* states. The conduction band minimum (CBM) is predominantly Nb 4*d* states with increasing O 2*p* states towards 6 eV. These results are consistent with other theoretical studies carried out on Nb₂O₅.

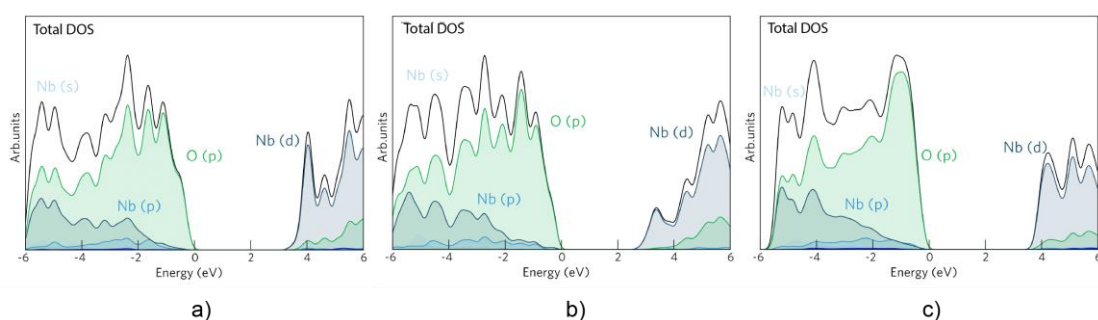


Figure 3: The calculated density of states (DOS) for a) orthorhombic b) tetragonal and c) monoclinic Nb₂O₅ systems. Each diagram displays the total density of states (black line) and the individual contributions of the elements and orbitals (coloured lines).

Despite much research being carried out on Nb₂O₅, few theoretical studies have been carried out to be accurate for electronic properties. The theoretical band gaps presented in the literature range from ~2.5-4.6 eV however the majority of studies use standard DFT functionals which are well known to underestimate the band gaps of materials. The calculated fundamental and optical band gaps in this work using the HSE06 functional and the band structures are displayed in Figure 4a-c with the calculated optical absorption spectra in Figure 4d-f where for each polymorph an indirect band gap is seen. The orthorhombic band structure (Figure 4a) has its VBM at the gamma high symmetry point (Γ) and CBM at the Y high symmetry point giving an indirect band gap of 4.05 eV. The optical transition occurs between Γ and X from the second highest valence band to the lowest conduction band ($E_g^{\text{opt}} = 4.16$ eV). The VBM and CBM in the tetragonal structure (Figure 4b) are found at N and Γ respectively giving rise to an indirect band gap of 3.16 eV. The optical transition in tetragonal Nb₂O₅ occurs at Γ with an optical band gap of 3.64 eV. Lastly, the monoclinic band structure (Figure 4c) shows the VBM at L and the CBM at Y with an indirect band gap of 3.67 eV. The direct band gap transition at L (VBM) is allowed and as such the optical band gap is 4.19 eV ($E_g^{\text{dir}} = E_g^{\text{opt}}$).

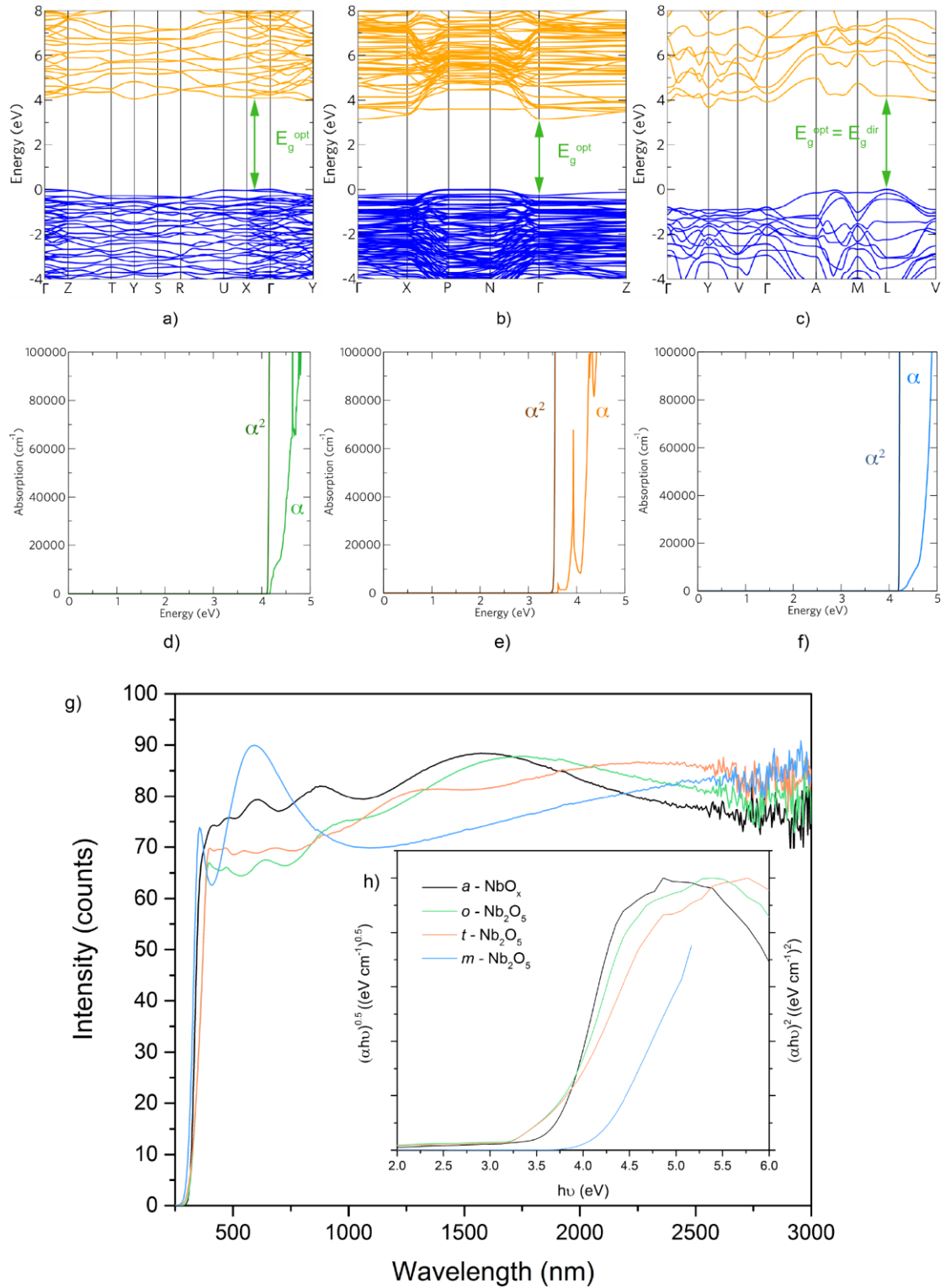


Figure 4: The calculated band structures for a) orthorhombic b) tetragonal and c) monoclinic Nb₂O₅. The valence and conduction bands are depicted with blue and orange bands respectively, and the optical transitions are displayed with the green arrow. d), e) and f) Show the calculated optical absorption spectra for *o*-, *t*- and *m*- Nb₂O₅ (respectively) summed over all possible direct valence to conduction band transitions. These spectra are calculated using the HSE06 functional. g) Displays UV – Vis spectra of the AACVD grown amorphous and annealed crystalline thin films on quartz. The insert h) shows the Tauc plot showing the indirect optical band gaps for *a*-, *o*- and *t*- Nb₂O₅ and the direct band gap for *m*- Nb₂O₅.

These theoretical results match well with the experimental optical properties determined from UV-Visible spectroscopy (Figure 4g) data, from which the Tauc plot was used to determine the optical indirect band gaps for *a*-, *o*-, *t*- Nb₂O₅ and the direct band for *m*- Nb₂O₅. The results of which are presented in Table 1. The experimental results for *t*- and *m*- Nb₂O₅ show excellent match to the theoretical results and are within the range observed in literature (3.10 -4.87 eV).

A recent study on monoclinic Nb₂O₅ (in the P2/m structure) was carried out using a modified Becke-Johnson functional, they found that their optical band gap was 3 eV (matching their experimentally defined band gap of 3.1-3.2eV).²⁶ Whilst they see an excellent correlation between theory and experiment, we find that the difference between the P2/m monoclinic structure (which contains 15 non-equivalent Nb sites) and the C2/m monoclinic structure (used in this study which contains 1 non-equivalent Nb site) makes a large difference in electronic structure. We have found that the HSE06 hybrid functional described the electronic structure of all three of our polymorphs to a high degree of accuracy and in direct agreement with our experimental values.

Table 1: The experimental band gap and refractive index at various wavelengths for the amorphous and annealed Nb₂O₅. The theoretical fundamental (E_g^{fund}) and optical (E_g^{opt}) band gaps for each phase of Nb₂O₅ using the HSE06 functional are also shown.

Film	Experimental E_g^{opt} / eV	Theoretical E_g^{fund} / eV	Theoretical E_g^{opt} / eV
<i>a</i> - Nb ₂ O ₅	3.8 (ind)	N/A	N/A
<i>o</i> - Nb ₂ O ₅	3.7 (ind)	4.05 (ind)	4.16
<i>t</i> - Nb ₂ O ₅	3.6 (ind)	3.16 (ind)	3.64
<i>m</i> - Nb ₂ O ₅	4.2 (dir)	3.67 (ind)	4.19

Conclusion

In conclusion we report, for the first time, the AACVD synthesis of amorphous Nb₂O₅ and subsequent annealing of the thin films on quartz to obtain the three most stable and useful polymorphs - orthorhombic, tetragonal and monoclinic. XPS analysis of the surface revealed the as-deposited film to contain Nb(IV) states as a result of oxygen vacancies. SEM images revealed the amorphous film to have densely packed nanostructure while the annealed samples had large features protruding from the substrate. Experimental optical characterization matched well with hybrid functional theory calculations. The calculated optical band gaps, which are usually underestimated by traditional DFT calculations, matched well to experimental values and those found in literature.

Experimental

Deposition Procedure

Depositions were carried out in N₂ (BOC Ltd., oxygen free nitrogen, 99.99% purity). [Nb(OEt)₅] precursor (99%) was placed in a glass bubbler along with dry methanol and an aerosol mist was created using a piezoelectric device (Johnson Matthey liquifog[®]). [Nb(OEt)₅] was procured from Aldrich and used as received. MeOH was also procured from Aldrich but dried over Mg and stored under molecular sieves before use.

[Nb(OEt)₅] (0.5 g, 1.57 mmol) was dissolved in MeOH (20 ml). The resulting solution was stirred for 10 minutes and then atomised. The precursor vapour was carried to the reactor using a constant N₂ flow of 0.5 L.min⁻¹. Films were grown on quartz slides placed on SiO₂ barrier coated float glass (Pilkington NSG). A top plate was suspended 0.5 cm above the glass substrate to ensure laminar flow. The deposition was conducted at 450 °C, where the substrate was heated on its underside using cartridge heaters embedded within a graphite block. The reaction took 60 minutes to complete. After the deposition the bubblers were closed and the substrates were allowed to cool under a flow of N₂ to less than 100 °C before it was removed. Coated substrates were handled and stored in air. The coated glass substrate was cut into ca. 1 cm × 1 cm squares for subsequent analysis.

Annealing Procedure

The Nb₂O₅ films on quartz were annealed in a Carbolite GLM 1 furnace with a Eurotherm 2216e temperature controller in air. Films were placed inside the oven at room temperature and heated to 800, 1000 or 1200 °C depending on the polymorph required, at a rate of 10 °C per minute, before being held at this temperature for 12 hrs. The furnace was allowed to cool to below 100 °C before the film was removed.

Film Characterisation

X-ray diffraction (XRD) patterns were measured in a modified Bruker-Axs D8 diffractometer with parallel beam optics and a PSD LynxEye silicon strip detector. This instrument uses an unmonochromated Cu K α source operated at 40 kV with 30 mA emission current. The incident beam angle was set at 0.5° and the angular range of the patterns collected was 10° < 2 θ < 65° with a step size of 0.05° counted at 1 s/step.

Scanning Electron Microscopy (SEM) was performed to determine surface morphology and film thickness using a JEOL JSM-6301F Field Emission SEM at an accelerating voltage of 5 keV.

Optical spectra were taken using a Perkin Elmer Fourier transform Lambda 950 spectrometer over a wavelength range of 190 nm to 3000 nm. This range encompasses the ultraviolet (UV), visible and near infrared (NIR) regions. The spectra were referenced against an air background.

X-ray photoelectron spectroscopy (XPS) was performed in a Thermo Scientific K-alpha photoelectron spectrometer using monochromatic Al-K α radiation. Survey scans were collected in the range 0–1100 eV (binding energy) at a pass energy of 160 eV. Higher resolution scans were recorded for the main core lines at a pass energy of 20 eV. Valence band spectra were also recorded. Peak positions were calibrated to adventitious carbon (284.5 eV) and plotted using the CasaXPS software.

Density Functional Theory

Density functional theory (DFT) calculations using the Vienna *ab-initio* Simulation Package (VASP)^{27–30} were used in order to investigate the electronic structures of three polymorphs of Nb₂O₅, (monoclinic – C2/m, orthorhombic – P2₁2₁2₁ and tetragonal – I₄/mmm), the unit cells of which are shown in Figure 5. The HSE06

(Heyd-Scuzeria-Ernzerhoff)³¹ screened hybrid functional was utilised to describe the structural and electronic properties of the three polymorphs. Hybrid functionals are generally more accurate than standard functionals, yielding improved geometries and electronic structures more consistent with experiment.^{32–36} Within HSE06 the exchange interaction is split into both short range (SR) and long range (LR) parts, with 25% of exact non-local Fock exchange being substituted into the short range PBE (Perdew-Burke-Ernzerhoff)³⁷ functional. A screening factor of 0.207 Å⁻¹ is applied to the short range and long range terms of the Coulomb potential resulting in:

$$E_{xc}^{HSE0} = E_x^{HSE06,SR} + E_x^{PBE,LR} + E_c^{PBE}$$

Where

$$E_x^{HSE06,SR} = \frac{1}{4} E_x^{Fock,SR} + \frac{3}{4} E_x^{PBE,SR}$$

The interactions between the core electrons (Nb[Kr] and O[He]) and the valence electrons were described using the Projector Augmented Wave Method (PAW).³⁸

For each Nb₂O₅ structure a plane wave energy cut-off of 600 eV was deemed sufficient for convergence alongside Γ -centred k-point meshes of 4 x 4 x 6 (monoclinic), 5 x 3 x 3 (orthorhombic) and 2 x 2 x 2 (tetragonal) for the 7, 28 and 56 atom cells respectively. Structural optimisations were carried out on each structure, relaxing the lattice vectors, cell angles, cell volumes and atomic positions. Convergence was deemed to be complete when all the forces on the atoms were less than 0.01 eV Å⁻¹. Optical absorption spectra were also calculated using optical transition matrix elements calculated within the transversal approximation and PAW method.³⁸ The absorption spectrum is summed over all direct valence band to conduction band transitions ignoring intraband and indirect absorptions.³⁹ Despite not addressing electron-hole correlation, this methodology has previously shown excellent agreement towards experimental absorption spectra.^{40–44}

In order to simulate the valence band X-ray photoelectron spectra (VB-XPS) and compare with the experimental data, the calculated density of states (DOS) was weighted using the atomic orbital photoionisation cross-sections formulated by Yeh and Lindau.²⁵ A Gaussian broadening of 0.47 eV was applied to match the broadening

observed in experiment. Multiple accounts have been shown of this method providing accurate descriptions of the states that make up the XPS data.^{22,35,44–46}

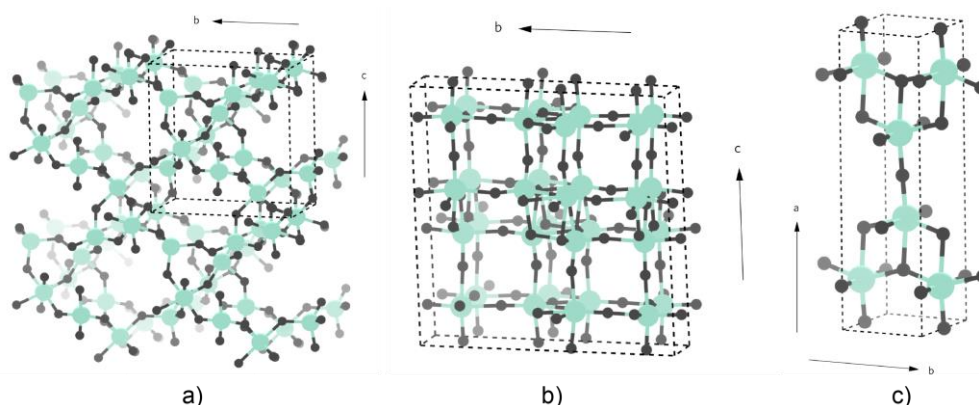


Figure 5: The unit cells of Nb_2O_5 in the a) monoclinic⁴⁷ structure ($C2/m$) b) orthorhombic⁴⁸ Structure ($P2_12_12_1$) and c) the tetragonal⁴⁹ structure ($I4/mmm$). The unit cell boundaries are portrayed with dashed black lines and the Nb and O atoms as teal and dark grey spheres respectively.

Acknowledgment

Thanks to Dr. Ainara Garcia Gallastegui for useful discussions. We thank the Deanship of Scientific Research (DSR), King Abdulaziz University, Jeddah for funding the work under grant D-1-434. Bio Nano Consulting and UCL are thanked for the Impact studentship for B.A.D.W. This work made use of the ARCHER UK National Supercomputing Service (<http://www.archer.ac.uk>), via our membership of the UK's HEC Materials Chemistry Consortium, which is funded by EPSRC (EP/L000202). The UCL Legion and Grace HPC Facilities (Legion@UCL and Grace@UCL) were also used in completion of this work.

Conflict of interest

S. Sathasivam was employed by BioNano Consulting Ltd.

References

- (1) Rani, R. A.; Zoolfakar, A. S.; O'Mullane, A. P.; Austin, M. W.; Kalantar-Zadeh, K. Thin Films and Nanostructures of Niobium Pentoxide: Fundamental Properties, Synthesis Methods and Applications. *J. Mater. Chem. A* **2014**, *2*, 15683–15703.
- (2) Wylezich, H.; Mähne, H.; Rensberg, J.; Ronning, C.; Zahn, P.; Slesazeck, S.; Mikolajick, T. Local Ion Irradiation-Induced Resistive Threshold and Memory Switching in Nb₂O₅/NbO_x Films. *ACS Appl. Mater. Interfaces* **2014**, *6* (20), 17474–17480.
- (3) Fu, Z.; Kong, J.; Qin, Q. Electrochemical and Electrochromic Properties of Niobium Oxide Thin Films Fabricated by Pulsed Laser Deposition. *J. Electrochem. Soc.* **1999**, *146* (10), 3914–3918.
- (4) Ghosh, R.; Brennaman, M. K.; Uher, T.; Ok, M.-R.; Samulski, E. T.; Mcneil, L. E.; Meyer, T. J.; Lopez, R. Nanoforest Nb₂O₅ Photoanodes for Dye-Sensitized Solar Cells by Pulsed Laser Deposition. *ACS Appl. Mater. Interfaces* **2011**, *3* (10), 3929–3935.
- (5) Blanquart, T.; Niinistö, J.; Heikkilä, M.; Sajavaara, T.; Kukli, K.; Puukilainen, E.; Xu, C.; Hunka, W.; Ritala, M.; Leskelä, M. Evaluation and Comparison of Novel Precursors for Atomic Layer Deposition of Nb₂O₅ Thin Films. *Chem. Mater.* **2012**, *24* (6), 975–980.
- (6) O'Neill, S. A.; Parkin, I. P.; Clark, R. J. H.; Mills, A.; Elliott, N. Atmospheric Pressure Chemical Vapour Deposition of Thin Films of Nb₂O₅ on Glass. *J. Mater. Chem.* **2003**, *13* (12), 2952–2956.
- (7) Velten, D.; Eisenbarth, E.; Schanne, N.; Breme, J. Biocompatible Nb₂O₅ Thin Films Prepared by Means of the Sol–gel Process. *J. Mater. Sci. Mater. Med.* **2004**, *15* (4), 457–461.
- (8) Luo, H.; Song, W.; Hoertz, P. G.; Hanson, K.; Ghosh, R.; Rangan, S.; Brennaman, M. K.; Concepcion, J. J.; Binstead, R. A.; Bartynski, R. A.; Lopez, R.; Meyer, T. J. A Sensitized Nb₂O₅ Photoanode for Hydrogen Production in a Dye-Sensitized Photoelectrosynthesis Cell. *Chem. Mater.* **2013**, *25* (2), 122–

- (9) Lenzmann, F.; Krueger, J.; Burnside, S.; Brooks, K.; Grätzel, M.; Gal, D.; Rühle, S.; Cahen, D. Surface Photovoltage Spectroscopy of Dye-Sensitized Solar Cells with TiO₂, Nb₂O₅, and SrTiO₃ Nanocrystalline Photoanodes: Indication for Electron Injection from Higher Excited Dye States. *J. Phys. Chem. B* **2001**, *105* (27), 6347–6352.
- (10) Yan, L.; Chen, G.; Sarker, S.; Richins, S.; Wang, H.; Xu, W.; Rui, X.; Luo, H. Ultrafine Nb₂O₅ Nanocrystal Coating on Reduced Graphene Oxide as Anode Material for High Performance Sodium Ion Battery. *ACS Appl. Mater. Interfaces* **2016**, *8* (34), 22213–22219.
- (11) Betzler, S. B.; Harzer, T.; Ciston, J.; Dahmen, U.; Dehm, G.; Scheu, C. Heat-Induced Phase Transformation of Three-Dimensional Nb₃O₇(OH) Superstructures: Effect of Atmosphere and Electron Beam. *Cryst. Growth Des.* **2016**, *16* (8), 4309–4317.
- (12) Wang, C.; Yin, L.; Zhang, L.; Xiang, D.; Gao, R. Metal Oxide Gas Sensors: Sensitivity and Influencing Factors. *Sensors*. 2010, pp 2088–2106.
- (13) Rani, R. A.; Zoolfakar, A. S.; Oua, J. Z.; Field, M. R.; Austin, M.; Kalantar-Zadeh, K. Nanoporous Nb₂O₅ Hydrogen Gas Sensor. *Sens. Actuator B - Chem* **2013**, *176*, 149–156.
- (14) Ab Kadir, R.; Rani, R. A.; Alsaif, M. M. Y. A.; Ou, J. Z.; Wlodarski, W.; O'Mullane, A. P.; Kalantar-Zadeh, K. Optical Gas Sensing Properties of Nanoporous Nb₂O₅ Films. *ACS Appl. Mater. Interfaces* **2015**, *7* (8), 4751–4758.
- (15) Braga, V. S.; Dias, J. a; Dias, S. C. L.; De Macedo, J. L. Catalyst Materials Based on Nb₂O₅ Supported on SiO₂ –Al₂O₃ : Preparation and Structural Characterization. *Chem. Mater.* **2005**, *17* (3), 690–695.
- (16) Ramakrishna, S.; Le Viet, A.; Reddy, M. V.; Jose, R.; Chowdari, B. V. R. Nanostructured Nb₂O₅ Polymorphs by Electrospinning for Rechargeable Lithium Batteries. *J. Phys. Chem. C* **2010**, *114* (1), 664–671.

- (17) Kumagai, N.; Tanno, K.; Nakajima, T.; Watanabe, N. Structural Changes of Nb₂O₅ and V₂O₅ as Rechargeable Cathodes for Lithium Battery. *Electrochim. Acta* **1983**, 28 (1), 17–22.
- (18) Lai, F.; Li, M.; Wang, H.; Hu, H.; Wang, X.; Hou, J. G.; Song, Y.; Jiang, Y. Optical Scattering Characteristic of Annealed Niobium Oxide Films. *Thin Solid Films* **2005**, 488 (1–2), 314–320.
- (19) Knapp, C. E.; Carmalt, C. J. Solution Based CVD of Main Group Materials. *Chem. Soc. Rev.* **2016**, 45 (4), 1036–1064.
- (20) Bhachu, D. S.; Sathasivam, S.; Carmalt, C. J.; Parkin, I. P. PbO-Modified TiO₂ Thin Films: A Route to Visible Light Photocatalysts. *Langmuir* **2014**, 30 (2), 624–630.
- (21) Sathasivam, S.; Arnepalli, R. R.; Singh, K. K.; Visser, R. J.; Blackman, C. S.; Carmalt, C. J. A Solution Based Route to GaAs Thin Films from As (NMe₂)₃ and GaMe₃ for Solar Cells. *RSC Adv.* **2015**, 5 (16), 11812–11817.
- (22) Bhachu, D. S.; Moniz, S. J. A.; Sathasivam, S.; Scanlon, D. O.; Walsh, A.; Bawaked, S. M.; Mokhtar, M.; Obaid, A. Y.; Parkin, I. P.; Tang, J.; Carmalt, C. J. Bismuth Oxyhalides: Synthesis, Structure and Photoelectrochemical Activity. *Chem. Sci.* **2016**, 7 (8), 4832–4841.
- (23) Hou, X.; Choy, K. L. Processing and Applications of Aerosol-Assisted Chemical Vapor Deposition. *Chem. Vap. Depos.* **2006**, 12 (10), 583–596.
- (24) Mittal, K. L. Adhesion Measurement of Thin Films. *Electrocompon. Sci. Technol.* **1976**, 3 (1), 21–42.
- (25) Yeh, J. J.; Lindau, I. Atomic Subshell Photoionization Cross Sections and Asymmetry Parameters: 1 [Less-than-or-Equals, Slant] Z [Less-than-or-Equals, Slant] 103. *At. Data Nucl. Data Tables* **1985**, 32 (1), 1–155.
- (26) Khan, W.; Betzler, S. B.; Šipr, O.; Ciston, J.; Blaha, P.; Scheu, C.; Minar, J. Theoretical and Experimental Study on the Optoelectronic Properties of Nb₃O₇(OH) and Nb₂O₅ Photoelectrodes. *J. Phys. Chem. C* **2016**, 7, acs.jpcc.6b06391.

- (27) Kresse, G.; Hafner, J. Ab Initio Molecular Dynamics for Liquid Metals. *Phys. Rev. B* **1993**, *47* (1), 558–561.
- (28) Kresse, G.; Hafner, J. Ab Initio Molecular-Dynamics Simulation of the Liquid-Metal-amorphous-Semiconductor Transition in Germanium. *Phys. Rev. B* **1994**, *49* (20), 14251–14269.
- (29) Kresse, G.; Furthmüller, J. Efficiency of Ab-Initio Total Energy Calculations for Metals and Semiconductors Using a Plane-Wave Basis Set. *Comput. Mater. Sci.* **1996**, *6* (1), 15–50.
- (30) Kresse, G.; Furthmu, J.; J., F.; Kresse, G.; Furthmu, J. Efficient Iterative Schemes for Ab Initio Total-Energy Calculations Using a Plane-Wave Basis Set. *Phys. Rev. B Condens. Matter Mater. Phys.* **1996**, *54* (16), 11169.
- (31) Heyd, J.; Scuseria, G. E.; Ernzerhof, M. Hybrid Functionals Based on a Screened Coulomb Potential. *J. Chem. Phys.* **2003**, *118* (18), 8207–8215.
- (32) Rajpalke, M. K.; Linhart, W. M.; Birkett, M.; Yu, K. M.; Scanlon, D. O.; Buckeridge, J.; Jones, T. S.; Ashwin, M. J.; Veal, T. D. Growth and Properties of GaSbBi Alloys. *Appl. Phys. Lett.* **2013**, *103* (14), 0–4.
- (33) Burbano, M.; Scanlon, D. O.; Watson, G. W. Sources of Conductivity and Doping Limits in CdO from Hybrid Density Functional Theory. *J. Am. Chem. Soc.* **2011**, *133* (38), 15065–15072.
- (34) Walsh, A.; Chen, S.; Wei, S. H.; Gong, X. G. Kesterite Thin-Film Solar Cells: Advances in Materials Modelling of $\text{Cu}_2\text{ZnSnS}_4$. *Adv. Energy Mater.* **2012**, *2* (4), 400–409.
- (35) Marchand, P.; Sathasivam, S.; Williamson, B. A. D.; Pugh, D.; Bawaked, S. M.; Basahel, S. N.; Obaid, A. Y.; Scanlon, D. O.; Parkin, I. P.; Carmalt, C. J. A Single-Source Precursor Approach to Solution Processed Indium Arsenide Thin Films. *J. Mater. Chem. C* **2016**.
- (36) Garza, A. J.; Scuseria, G. E. Predicting Band Gaps with Hybrid Density Functionals. *J. Phys. Chem. Lett.* **2016**, *7*, 4165–4170.
- (37) Perdew, J. P.; Burke, K.; Ernzerhof, M. Generalized Gradient Approximation

- Made Simple. *Phys. Rev. Lett.* **1996**, *77* (18), 3865–3868.
- (38) Blochl, P. E. Projector Augmented-Wave Method. *Phys. Rev. B* **1994**, *50* (24), 17953–17979.
- (39) Adolph, B.; Furthmüller, J.; Bechstedt, F. Optical Properties of Semiconductors Using Projector-Augmented Waves. *Phys. Rev. B* **2001**, *63* (12), 125108.
- (40) Nie, X.; Wei, S.-H.; Zhang, S. B. Bipolar Doping and Band-Gap Anomalies in Delafossite Transparent Conductive Oxides. *Phys. Rev. Lett.* **2002**, *88* (6), 66405.
- (41) Walsh, A.; Da Silva, J. L. F.; Yan, Y.; Al-Jassim, M. M.; Wei, S.-H. Origin of Electronic and Optical Trends in Ternary In₂O₃(ZnO)_n Transparent Conducting Oxides (n=1,3,5): Hybrid Density Functional Theory Calculations. *Phys. Rev. B* **2009**, *79* (7), 73105.
- (42) Godinho, K. G.; Carey, J. J.; Morgan, B. J.; Scanlon, D. O.; Watson, G. W. Understanding Conductivity in SrCu₂O₂: Stability, Geometry and Electronic Structure of Intrinsic Defects from First Principles. *J. Mater. Chem.* **2010**, *20* (6), 1086–1096.
- (43) Allen, J. P.; Scanlon, D. O.; Piper, L. F. J.; Watson, G. W. Understanding the Defect Chemistry of Tin Monoxide. *J. Mater. Chem. C* **2013**, *1* (48), 8194.
- (44) Williamson, B. A.; Buckeridge, J.; Brown, J.; Ansbro, S.; Palgrave, R. G.; Scanlon, D. O. Engineering Valence Band Dispersion for High Mobility P-Type Semiconductors. *Chem. Mater.* **2016**, *acs.chemmater.6b03306*.
- (45) Savory, C. N.; Ganose, A. M.; Travis, W.; Atri, R. S.; Palgrave, R. G.; Scanlon, D. O. An Assessment of Silver Copper Sulfides for Photovoltaic Applications: Theoretical and Experimental Insights. *J. Mater. Chem. A* **2016**, *4* (32), 12648–12657.
- (46) Sathasivam, S.; Arnepalli, R. R.; Bhachu, D. S.; Lu, Y.; Buckeridge, J.; Scanlon, D. O.; Kumar, B.; Singh, K. K.; Visser, R. J.; Blackman, C. S.; Carmalt, C. J. Single Step Solution Processed GaAs Thin Films from GaMe₃ and T BuAsH₂ under Ambient Pressure. *J. Phys. Chem. C* **2016**, *120* (13),

7013–7019.

- (47) Gruehn, R. Eine Weitere Neue Modifikation Des Niobpentoxids. *J. Less Common Met.* **1966**, *11* (2), 119–126.
- (48) Jain, A.; Ong, S. P.; Hautier, G.; Chen, W.; Richards, W. D.; Dacek, S.; Cholia, S.; Gunter, D.; Skinner, D.; Ceder, G. Commentary: The Materials Project: A Materials Genome Approach to Accelerating Materials Innovation. *Apl Mater.* **2013**, *1* (1), 11002.
- (49) Mertin, W.; Andersson, S.; Gruehn, R. Über Die Kristallstruktur von M-Nb₂O₅. *J. Solid State Chem.* **1970**, *1* (3–4), 419–424.

Table of Contents Graphic

